2019

Wind-induced ground motion: dynamic model and non-uniform structure for ground

Mohammad Mohammadi
University of Mississippi, mmohamm1@go.olemiss.edu

Craig J. Hickey
University of Mississippi, chickey@olemiss.edu

Richard Raspet
University of Mississippi, raspet@olemiss.edu

Vahid Naderyan
University of Mississippi

Recommended Citation

Mohammadi, M., Hickey, C. J., Raspet, R., & Naderyan, V. (2019). Wind-induced ground motion: Dynamic model and nonuniform structure for ground. Journal of Geophysical Research: Solid Earth, 124. https://doi.org/10.1029/2019JB017562

JGR Solid Earth

RESEARCH ARTICLE
10.1029/2019JB017562

Key Points:
- Two generalizations on a previous method for predicting ground vibrations caused by wind are investigated
- A dynamic model for wind-induced ground motion is developed
- The wind-induced surface deformations of three different types of nonuniform grounds are predicted

Correspondence to:
M. Mohammadi,
m.mohammadi@outlook.com

Citation:
Mohammadi, M., Hickey, C. J., Raspet, R., & Naderyan, V. (2019). Wind-induced ground motion: Dynamic model and nonuniform structure for ground. *Journal of Geophysical Research: Solid Earth*, *124*. https://doi.org/10.1029/2019JB017562

Received 23 FEB 2019
Accepted 17 JUL 2019
Accepted article online 27 JUL 2019

Wind-Induced Ground Motion: Dynamic Model and Nonuniform Structure for Ground

M. Mohammadi[1], C. J. Hickey[1], R. Raspet[1], and V. Naderyan[1]

[1]National Center for Physical Acoustics, University of Mississippi, Oxford, MS, USA

Abstract Wind-induced ground vibrations are a source of noise in seismic surveys. In a previous study, a wind-ground coupling theory was developed to predict the power spectral density of ground motions caused by wind perturbations on the ground surface. The prediction was developed using a superposition of the point source response of an elastic isotropic homogeneous medium deforming quasi-statically with the statistical description of the wind-induced pressure fluctuations on the ground. Model predictions and field measurements were in agreement for the normal component of the displacement but underpredicted the horizontal component. In this paper, two generalizations are investigated to see if they lead to increased horizontal displacement predictions: (1) First, the dynamic point source response is calculated and incorporated into the ground displacement calculation. Measured ground responses are used to incorporate losses into the dynamic calculation. (2) The quasi-static response function for three different types of nonuniform grounds are calculated and used in the seismic wind noise superposition. The dynamic point source response and the three more realistic ground models result in larger horizontal displacements for the point source at distances on the order of 1 m or greater from the source. However, the superposition to predict the seismic wind noise is dominated by the displacements very close to the point source where the prediction is unchanged. This research indicates that the modeling of the wind-induced pressure source distribution must be improved to predict the observed equivalency of the vertical and horizontal displacements.

1. Introduction

Wind noise is a source of seismic vibrations that obscure or mask seismic data. Understanding and predicting this noise source is an important step in reducing its effects. Furthermore, predicting these effects can help us to recognize or filter the desired data and avoid misunderstandings from the masked data. Wind noise on buried or flush seismic sensors can be attributed to the ground vibrations generated by the turbulent pressure and shear stress of the wind on the ground surface. In other words, wind is a distribution of vertical and possibly horizontal surface loads that shake the ground and obscure the desirable seismic phenomena that we want to observe. In this study, the main purpose is to understand the wind-ground coupling by developing a prediction model for the ground motion due to wind.

Naderyan et al. (2016) developed a prediction of the ground displacements spectra from the measured ground properties and predicted pressure and shear stress at the ground surface. The prediction was based on Yu et al. (2011) theory for the prediction of the pressure fluctuation spectrum at the ground surface from the wind velocity spectrum. The second factor necessary for predicting the ground deformation is a model of the deformation of the ground due to point sources on the ground surface. Naderyan et al. (2016) modeled the ground as a linearly elastic half-space bounded by an infinite plane on one side. The wind excitation over the ground surface is a slowly moving fluctuation of pressure so the ground displacements were assumed to occur quasi-statically. The deformation of the ground due to the point forces were determined from Landau and Lifshitz (1986). The net ground deformations at a measurement point are due to a distribution of sources for wind turbulence over the ground surface. The statistical distribution of sources due to the pressure fluctuation is characterized by the longitudinal and transverse correlation functions of the turbulence taken from Shields (2005).

Naderyan et al. (2016) acquired measurements under different wind speeds to compare with theoretical results. The predicted and measured vertical ground displacements agreed very well. However, the horizontal ground displacements were significantly underpredicted. It was postulated that the shear stress must be of the same order of magnitude as the normal pressure on the ground surface to explain the data. Subsequent to the Naderyan et al. (2016) publication, improvements to the calculation of the shear stress were investigated. None of the improvements predicted shear stresses large enough to account for the horizontal seismic wind noise data, but this study did lead to insight into the physical limitation on the magnitude of shear stresses. The source of molecular viscosity is the transport of horizontal momentum by random molecular motion (Reif, 1965). In the atmosphere, effective viscosity is caused by the transport of average horizontal momentum by the vertical turbulent fluctuations (Panofsky & Dutton, 1984). Estimation of the horizontal momentum density above the surface shows that the density is so low that no plausible mechanism can provide the vertical velocity or displacement large enough to lead to shear stresses on the order of the pressure fluctuations.

Motivated by this finding, an investigation of elastodynamic deformations of the ground (in lieu of the quasi-static theory) and nonuniform ground models (in lieu of the homogeneous isotropic ground model) was conducted to determine if the large observed horizontal displacements can be predicted from purely pressure fluctuation excitations (Mohammadi, 2018). The investigation of the elastodynamic response is motivated by the observation that the Rayleigh wave consists of both vertical and horizontal components whose ratio depends on material properties and depth. Reflections of compressional and shear waves from layers with different material properties leads to coupling between the waves and the conversion of pure P waves into reflected P and SV waves. Three different ground models are investigated to see if the horizontal component of the displacement due to a point force is enhanced by the inhomogeneity and, if so, whether this leads to a larger horizontal displacement in the wind-ground coupling model.

Section 2 describes the calculation of the ground displacements from the predicted wind turbulence-induced pressure fluctuation from Naderyan et al. (2016). Section 3.1 extends the calculation to include the dynamic response of the elastic half-space. Section 3.2 compares the theory to field measurement from a controlled source. The results of the measurement are then used in section 3.3 to incorporate viscoelasticity into the prediction, and in section 3.4 the result is compared to the measured seismic wind noise. Section 4 investigates three different inhomogeneous ground models. Section 4.1 investigates the wind noise coupling for a ground with continuously increasing rigidity. Section 4.2 studies the effect of a softer soil layer above a harder soil half-space. Finally, the coupling is calculated for a cross-anisotropic ground. Section 5 presents the conclusions of this study.

2. Wind-Ground Theory

Combining the theories discussed in the introduction leads to the following equations for the power spectra of the vertical and horizontal components of the wind-induced ground surface displacements due to the vertical pressure (Naderyan et al., 2016),

$$|U_r(k)|^2 = \int_{-\infty}^{\infty}\int_{-\infty}^{\infty}\int_{-\infty}^{\infty}\int_{-\infty}^{\infty} u_r(r)u_r(r')p_z^2(k)R_{(x-x')}R_{(y-y')}\mathrm{d}x\mathrm{d}x'\mathrm{d}y\mathrm{d}y', \tag{1a}$$

$$|U_z(k)|^2 = \int_{-\infty}^{\infty}\int_{-\infty}^{\infty}\int_{-\infty}^{\infty}\int_{-\infty}^{\infty} u_z(r)u_z(r')p_z^2(k)R_{(x-x')}R_{(y-y')}\mathrm{d}x\mathrm{d}x'\mathrm{d}y\mathrm{d}y', \tag{1b}$$

where U_r and U_z are horizontal and vertical displacements at the observation point of the pressure. k is wind pressure wave number. u_r and u_z are predicted horizontal and vertical displacements of the ground surface due to a unit vertical surface point force (per Newton); (x, y) and (x', y') are coordinates of two random points on the ground surface with respect to the observation point of the pressure; r and r' are $\sqrt{x^2+y^2}$ and $\sqrt{x'^2+y'^2}$, respectively; and $p_z^2(k)$ is the power spectral density (PSD) of wind pressure on the ground at wave number k which is obtained from the prediction model by Yu et al. (2011). $R_{(x-x')}$ and $R_{(y-y')}$ are wave number-dependent correlation functions of the wind in the downwind and crosswind directions, respectively. The proposed correlation functions by Shields (2005) are

$$R_{(x-x')} = \exp\left(-\alpha\frac{k}{2\pi}|x-x'|\right)\cos(k|x-x'|), \tag{2a}$$

$$R_{(y-y')} = \exp\left(-\beta\frac{k}{2\pi}|y-y'|\right). \tag{2b}$$

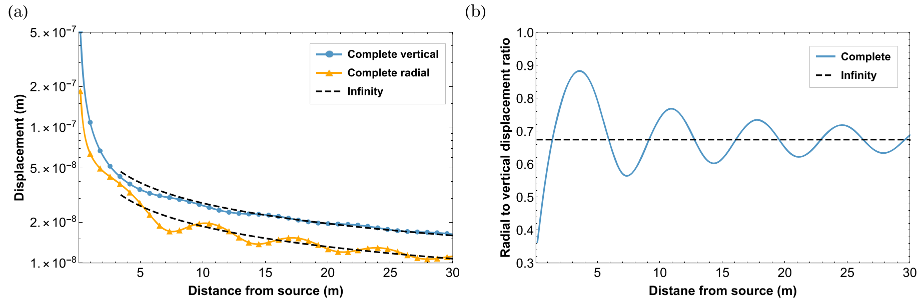

Figure 1. (a) Analytical surface displacements and (b) radial to vertical displacement ratio of an elastic half-space subjected to 50 Hz vertical surface load.

Shields' measurements evaluated α and β as 3.2 and 7.0, respectively, over a range of wind velocities (from 4 to 8 m/s) and different atmospheric and environmental conditions.

3. Dynamic Model for the Ground

In the work of Naderyan et al. (2016), the wind excitation over the ground surface was assumed to be a slowly moving fluctuation of pressure and shear stress. Assuming small accelerations, the ground displacements were considered mainly quasi-static. However, at higher frequencies the motion of the ground may deviate from the quasi-static assumption. This section investigates a new model using the same method for predicting the wind pressure fluctuations and correlation functions as Naderyan's study but incorporates the dynamic response for the ground. In the dynamic theory, the ground is modeled as an elastic or viscoelastic homogeneous half-space excited by wind pressure fluctuations characterized as a distribution of harmonic point forces acting on the surface.

The first analytical solution for the dynamic ground response subjected to a surface or an internal source was obtained mathematically by Lamb (1904) for a semi-infinite isotropic elastic solid subjected to vertical and horizontal concentrated surface forces. Lamb's theory predicts vertical and horizontal displacements of the same order of magnitude in the far field. The solution involves an evaluation of Cauchy principal integrals and of certain infinite integrals with oscillatory integrands. To evaluate the integrals, Barkan (1960) and Ewing et al. (1957) used corresponding Taylor series to study the radial and vertical components of the displacement. Since body waves play a significant role in the near-field response for this investigation, the accurate solution requires the numerical evaluation of Cauchy principal integrals which is accessible with current mathematical software.

The following section describes the dynamic model for the ground deformations. A field experiment is designed and conducted to illustrate the difference between the theoretical dynamic model of the ground and reality. The dynamic model is further improved by adding viscoelastic losses to the model. Finally, the dynamic wind-ground predictions are obtained and improvements and conclusions are illustrated by making a comparison with the measurements and with the previous quasi-static model.

3.1. Theory

The ground model is assumed to be an elastic isotropic solid occupying a half-space under the influence of a harmonic vertical point force on the surface. Assuming a concentrated harmonic force normal to the surface, $F_z e^{i\omega t}$, and applying the boundary conditions, the resulting equations for the surface displacements at a radius of r (Lamb, 1904) are

$$u_r = -\frac{F_z \kappa}{2G} H D_1(\kappa r) e^{i\omega t} + \frac{iF_z k^2}{\pi G} \int_h^k \frac{\xi^2(2\xi^2 - k^2)\alpha\beta}{F(\xi) f(\xi)} D_1(\xi r) e^{i\omega t} \mathrm{d}\xi, \tag{3a}$$

Table 1
Load and Ground Parameters

Load amplitude F_z	Load frequency $\omega/2\pi$	P wave velocity V_p	S wave velocity V_s	Density ρ	First Lamé Parameter	Shear modulus G
50 N	50 Hz	300 m/s	170 m/s	2,000 kg/m^3	64.4 MPa	57.8 MPa

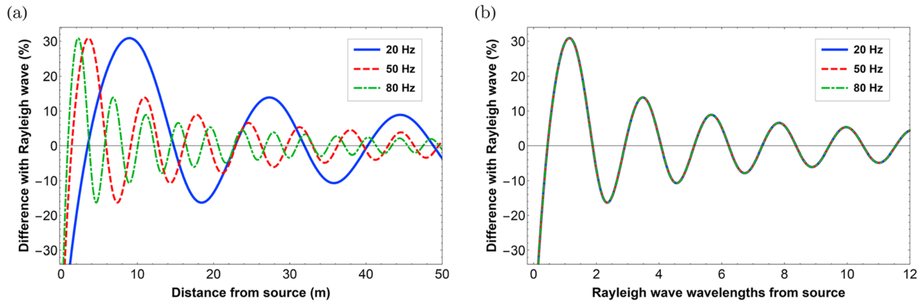

Figure 2. Percentage difference between radial to vertical displacement ratio of the complete solution and solution at infinity versus (a) range and (b) normalized range with Rayleigh wave wavelength for an elastic half-space subjected to 20, 50, and 80 Hz vertical surface load.

$$u_z = -\frac{iF_z k^2}{2\pi G}\mathrm{PV}\int_k^\infty \frac{\xi\alpha}{F(\xi)}D_0(\xi r) - \frac{iF_z k^2}{2\pi G}\int_h^k \frac{\xi(2\xi^2-k^2)^2\alpha}{F(\xi)f(\xi)}D_0(\xi r)e^{i\omega t}\mathrm{d}\xi, \tag{3b}$$

where F_z is the amplitude of the harmonic load, G is shear modulus, and κ is Rayleigh wave wavenumber. The other symbols are defined as follows:

$$F(\xi) = (2\xi^2 - k^2)^2 - 4\xi^2\alpha\beta, \tag{4}$$

$$\alpha^2 = \xi^2 - h^2, \qquad \beta^2 = \xi^2 - k^2, \tag{5}$$

$$h = \frac{\omega}{V_p}, \qquad k = \frac{\omega}{V_s}, \tag{6}$$

where V_p and V_s are the compressional (P wave) and shear wave (S wave) velocities in the ground. PV means "the principal value of," and D is defined as

$$D_n(\zeta) = -Y_n(\zeta) - iJ_n(\zeta), \tag{7}$$

where J_n and Y_n are the nth order Bessel functions of first and second kinds, respectively. H is defined as

$$H = -\frac{\kappa(2\kappa^2 - k^2 - 2\alpha_\kappa\beta_\kappa)}{F'(\kappa)} \tag{8}$$

for the dynamic ground response subjected to a surface or an internal source. Here α_κ and β_κ are α and β at $\xi = \kappa$, and F' is the derivative of F with respect to ξ. In equation (3a), the first term represents the Rayleigh wave with the wave number κ and the second term represents an aggregation of waves with the wave number range from h, P wave, to k, S wave. The second term decays faster than the first term with range because

Figure 3. Experiment setup with shaker and geophone array.

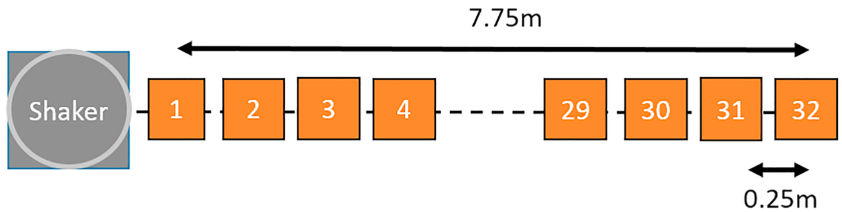

Figure 4. Diagram showing relative locations of geophones and shaker.

the Bessel function has a factor of r in the integral; this means that at great distances from the source the first term or the Rayleigh wave term dominates the displacement. This phenomenon is consistent with the geometrical spreading of the waves; Rayleigh waves spread in a two-dimension space, while body waves spread in a three-dimension space. The same form of equation can be obtained for the vertical component through a complex solution breaking the principal integral to simpler terms.

Lamb developed expressions for the Rayleigh wave terms at long distance from the source:

$$u_r = -\frac{iF_z\kappa}{2G}H\sqrt{\frac{2}{\pi\kappa r}}e^{i(\omega t-\kappa r-\frac{\pi}{4})}, \tag{9a}$$

$$u_z = \frac{F_z\kappa}{2G}K\sqrt{\frac{2}{\pi\kappa r}}e^{i(\omega t-\kappa r-\frac{\pi}{4})}, \tag{9b}$$

where

$$K = -\frac{k^2\alpha_\kappa}{F'(\kappa)}. \tag{10}$$

From equation (9), for free Rayleigh waves at long distances from the source, the magnitude of the ratio of horizontal to vertical displacement is H/K, which is constant. However, this ratio near the source is different and must be calculated considering the complete solution. Example calculations of the horizontal and vertical surface displacements and the horizontal to vertical ratio are displayed for the complete solution and the Rayleigh wave contributions for a ground in Figure 1. The source and soil properties used are listed in Table 1.

The displacement amplitudes do not decay monotonically in proportion to distance from the source, because of the interference of wave contributions in the near field (Barkan, 1960). As the radial distance increases, the amplitudes of the body waves decrease faster than the Rayleigh wave. Hence, the displacement amplitudes converge to the amplitude of the Rayleigh wave at infinity.

Figure 2a displays the percent difference of the radial to vertical displacement ratio between the complete solution and the solution at infinity for 20, 50, and 80 Hz sources versus range. At higher frequencies, the difference decreases faster with range and the complete solution converges to the Rayleigh wave values at shorter distances from the source. Normalizing the range based on the Rayleigh wave wavelength indicates that all sources with different frequencies have the same behaviors as shown in Figure 2b. Defining far field as a distance in which the difference between the complete solution and the solution at infinity is less than 5%, the boundary of the far field is 10 wavelengths from the source. Note that the ratio between the horizontal and vertical displacements is much larger than the comparable ratio for a static load at moderate distances from the source but is very small inside 0.4 Rayleigh wavelengths.

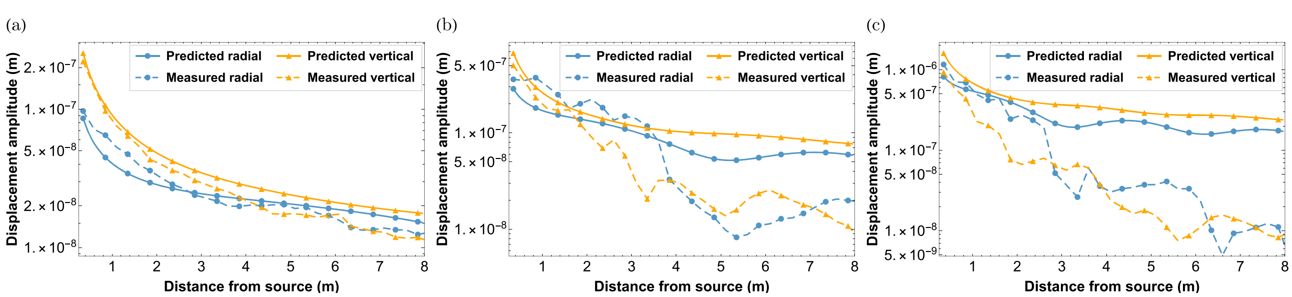

Figure 5. Predicted and measured surface displacements due to (a) 20, (b) 50, and (c) 80 Hz harmonic loads.

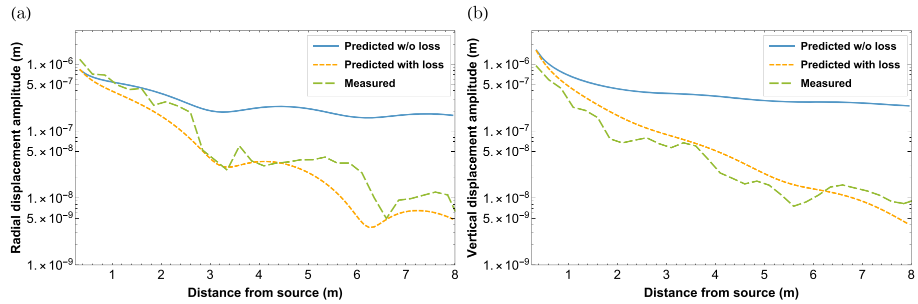

Figure 6. Predicted and measured (a) radial and (b) vertical surface displacements due to 80 Hz harmonic load.

3.2. Experiment

A set of field measurements were designed and conducted using a mechanical shaker in order to compare with the analytic model of the ground under the influence of a harmonic surface load. A vibrating shaker and a radial line of geophones from the shaker were used as a surface load and observation points, respectively, as shown in Figure 3. This experiment was conducted on a flat surface of an agricultural field near Locke Station, MS. Standard seismic refraction measurements were performed to provide the ground characterization at the site. These measurements provided *P* wave and *S* wave velocities of 220 and 120 m/s, respectively. The density of the ground was measured in the laboratory on a controlled volume of the soil. The weight of the soil sample was divided by its volume to calculate the density. The wet bulk density of the ground was approximately 2,180 kg/m^3.

The harmonic load was applied by a Vibration Test Systems VG-100-6 shaker placed level on the ground. The dimensions of the shaker are $H30 \times W25 \times D22$ cm with a mass of 30 kg. A sine wave created by a function generator and an amplifier acted as the shaker controller. A line of 24 geophones was planted at 25-cm spacing on the ground surface in a radial line from the shaker as shown in Figure 3. Figure 4 shows a diagram of the relative location of the geophones with respect to the shaker. The geophones were RTC 4.5 Hz, three-component, with 375-ohm windings. Each geophone box contains two perpendicular horizontal and one vertical geophone element. Each geophone has three 7-cm steel spikes on the bottom for coupling to the ground. Outputs from the geophones were connected to four 24-channel Geometrics Geode seismographs. For data acquisition, Geometrics Multiple Geode Operating Software recorded data from the Geode channels to a computer.

The measurements were acquired at different frequencies from 10 to 100 Hz. During each measurement, the geophones recorded 1,000 samples per second for 15 s with the shaker running at a constant frequency. The geophone outputs are converted to the ground displacements using the geophone transfer function. In order to compare experimental and the predicted ground deformations, the amplitude of the force on the surface is needed. The harmonic load amplitude at each frequency is determined by matching the measured value of the geophone closest to the source to the theoretical predicted load. Since the calculated load amplitudes from the vertical and horizontal displacements are different by 20% to 40%, their mean value is used in predictions. A comparison between the measured and predicted amplitude of the displacements versus

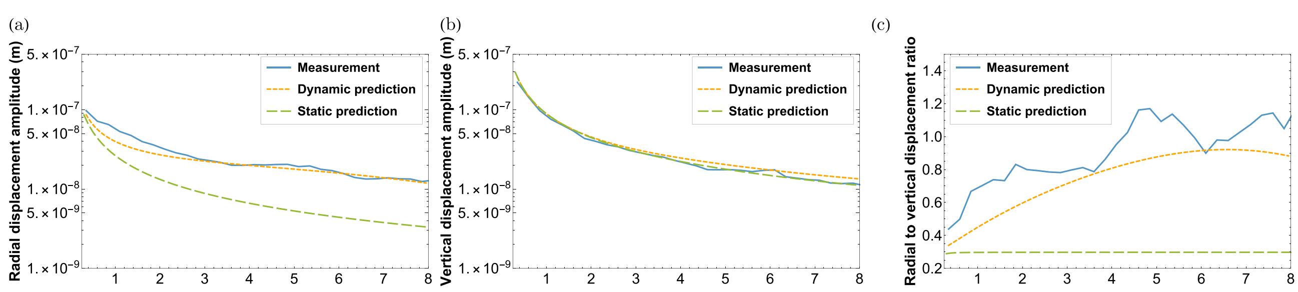

Figure 7. (a) Radial and (b) vertical displacements and (c) radial to vertical displacement ratio due to static and 20 Hz vertical surface loads.

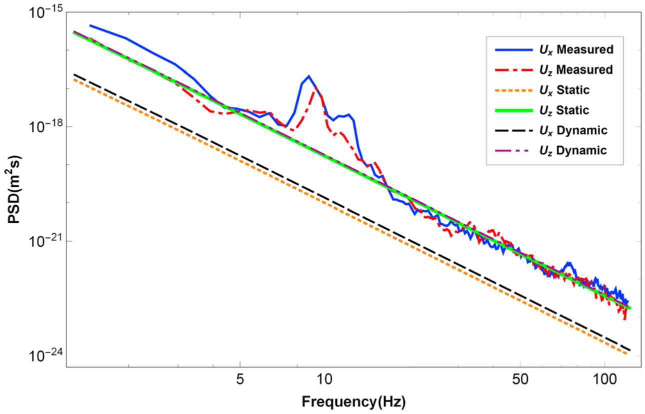

Figure 8. Measured and predicted wind-induced ground displacements using dynamic and static models. PSD = power spectral density.

the distance from the shaker is shown in Figure 5 for three different load frequencies. There are general similarities in their trends (increasing and decreasing versus range); however, they do not match. The difference between the measured and predicted values increases with increasing distance from the source. In addition, the difference and change with range increases with increasing frequency from 20 to 80 Hz. This means that the measured amplitudes decay faster than the predicted values as a function of range and the rate of attenuation increases as a function of frequency. This can be expected since there are other sources of attenuation in real soil in addition to the geometrical attenuation accounted for in the theory.

To account for the additional losses, a linear viscoelastic model is introduced using complex moduli. In equation (11), the loss factor η is defined to be linearly dependent on the frequency for the elastic modulus of the ground model. Using trial and error, the following elastic parameters are chosen as a good fit to the experimental data:

$$\eta = 0.003f \qquad G = G_0(1 + i\eta) \qquad \lambda = \lambda_0(1 + i\eta), \tag{11}$$

where G_0 and λ_0 are the original shear modulus and Lamé first parameter, respectively. The dynamic solution, equation (3), is solved for the viscoelastic ground model with the complex parameters, and its predictions are compared with the elastic model as well as the measured values for the displacement amplitudes. In Figure 6, the agreement between the viscoelastic model and measurements is shown at 80 Hz, particularly for the radial displacements. The viscoelastic ground model is significantly closer to the reality than the ideal elastic model.

3.3. Static Versus Dynamic Model

The static surface displacement of the elastic homogeneous half-space model of the ground under the influence of a vertical static point force on the surface is given by Landau and Lifshitz (1986),

$$u_r = \frac{(1+\nu)(1-2\nu)}{2\pi E}\frac{1}{r}F_z, \tag{12a}$$

$$u_z = \frac{(1+\nu)(1-\nu)}{\pi E}\frac{1}{r}F_z. \tag{12b}$$

As equation (12) shows, both components of the displacements are decaying functions of $1/r$. Figure 7 shows the surface displacements and the radial to vertical ratio of the static and dynamic predictions with losses and the measured values at 20 Hz. The static displacements decay monotonically with increasing range, whereas the measurements and dynamic predictions display nonmonotonic decay. The radial to vertical displacement ratio of the dynamic and static predictions are small and similar close to the source. The static deformation ratio is only a function of Poisson's ratio and remains constant with range, whereas the dynamic ratio has an oscillatory behavior like the measurements. The difference between the static and dynamic predictions, especially the increasing displacement ratio of the dynamic prediction away from the source, suggests that using the dynamic ground model may produce a better prediction of measured horizontal displacements due to the wind.

3.4. Dynamic Wind-Ground Model

In the study by Naderyan et al. (2016) the closed form expressions for the static ground deformations given by equation (12) were inserted into the wind-ground equation (equation (1)). Numerical integration (over truncated ranges) was used to calculate the PSD. For the dynamic case, the displacements given by equation (3) do not have a closed form solution that can be used in the numerical integration. However, the

Table 2
Simulation Parameters for Ground Model With Increasing Rigidity

Initial Young's modulus E_0	Poisson's ratio	Density
10 MPa	0.34	1,995 kg/m^3

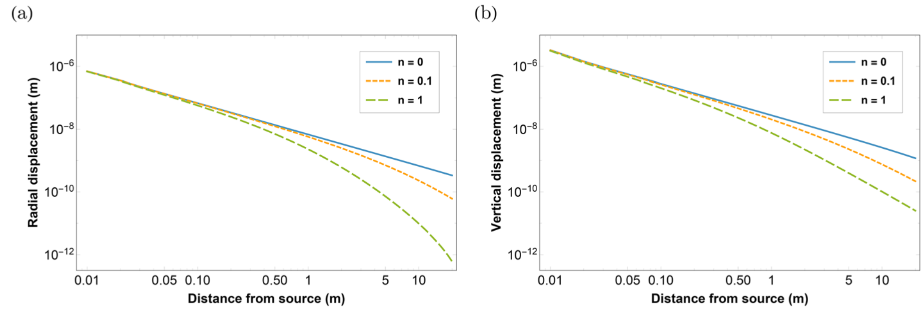

Figure 9. (a) Radial and (b) vertical surface displacements of ground models with different rates of continuously increasing rigidity due to a unit vertical surface load.

theoretical solution can be calculated at a finite number of points on a radial line from the source and an interpolation function can be used to represent the dynamic response function. This function is applied in the wind-ground equations, and the revised version of the integrals is numerically computed by Wolfram Research Inc. (2018). Comparison of the predictions using the viscoelastic dynamic model, the quasi-static model, and the measured values for the ground displacements are shown in Figure 8. The vertical components of both predictions match very well and are in a good agreement with the experiment. Although the horizontal displacements of the dynamic model are slightly larger than the static predictions, there is still a significant discrepancy between the predicted and measured displacements. The previous study showed that the predicted PSD of the vertical displacements due to the normal pressure was about 17 times greater than the horizontal, whereas the experimental values were very close. In this study, applying the dynamic model reduces the ratio to about 11, without changing the vertical component.

The ground deformations predicted by the static model, equation (12), or dynamic model, equation (3), are fast-decaying functions of range approaching infinity at the center $(r = 0)$. The wind correlation function is also a rapidly decreasing function of distance. These two factors make the wind-ground integration sensitive to the near field where the vertical displacements are significantly larger than the horizontal for both static and dynamic responses so the integrated wind noise differences are smaller than the difference observed in the point source response functions. In addition, the PSDs of the wind noise are proportional to the displacement squared so that differences in magnitude are amplified relative to the displacements.

4. Nonuniform Ground Model

This section generalizes the analysis of Naderyan et al. (2016) to include influences of the inhomogeneity and anisotropy of the ground on the wind-ground predictions. The goals are twofold: to evaluate the sensitivity of wind-ground measurements to layering in ground properties and to investigate if the difference between the predicted and measured horizontal displacement of the ground due to wind can be attributed to such nonuniformities.

In natural grounds, the stiffness usually increases with depth due to the increasing overburden pressure. Therefore, an elastic half-space model in which the rigidity increases as some function of depth can be a

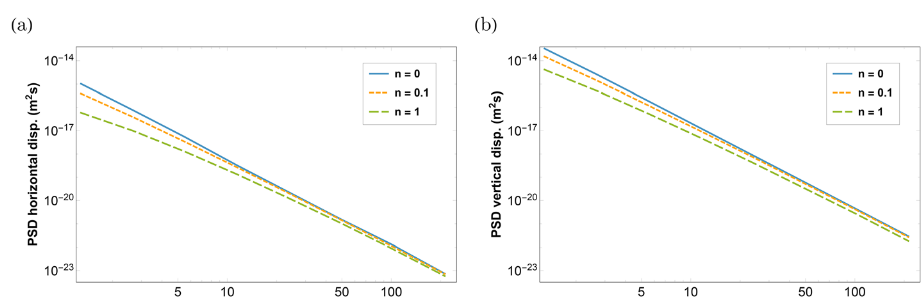

Figure 10. Predicted (a) horizontal and (b) vertical wind-induced displacements for ground models with different rates of continuously increasing rigidity. PSD = power spectral density.

Table 3
Layered Ground Model Parameters

Young's modulus			
Soft soil	Hard soil	Poisson's ratio	Density
50 MPa	100 MPa	0.34	1,995 kg/m^3

better approximation for the ground. Kassir (1970), Booker et al. (1985), and Oner (1990) considered an idealized elastic half-space in which the shear modulus or Young's modulus has a power law dependence on depth but the Poisson's ratio remains constant. In other cases, it is assumed that the ground consists of a limited number of distinct finite elastic layers of infinite lateral extent. The elastic properties (i.e., Poisson's ratio and shear modulus) are constant within each elastic layer but are different for any two connected layers. Yue and Wang (1988), Ernian (1989), and Pan et al. (2007) idealized the ground as a series of elastic layers over an elastic isotropic half-space. The effects of deposition and overburden can make the ground both inhomogeneous and anisotropic. From the practical engineering point of view, anisotropy of the ground is often modeled as a cross-anisotropic (transversely isotropic) half-space. Gerrard (1982) and Wang et al. (2006) developed an analytical ground model, associated with different loading scenarios, involving the stresses and displacements of a transversely isotropic half-space.

In this study, two inhomogeneous models are considered: a half-space with linearly increasing Young's modulus with depth (Booker et al., 1985; Kassir, 1970; Oner, 1990) and a single elastic layer over an elastic homogeneous half-space (Ernian, 1989; Pan et al., 2007; Yue & Wang, 1988). An anisotropic half-space with different elastic moduli in the vertical and radial directions (transversely isotropic) is also investigated (Gerrard, 1982; Wang et al., 2006). The surface displacements of these models as a function of radial distance from the source are required for input in the wind-ground integral equation. Since there is no closed form response function for these nonuniform models, a finite element approach is developed in COMSOL Multiphysics® to calculate the surface displacements due to a vertical surface load. The response functions (at discrete distances from the source) are interpolated between the computed data points for use in the wind-ground model. A comparison between the uniform and nonuniform predictions provides insight into the generalizations of the ground model on the wind-induced seismic behavior of the ground surface.

4.1. Continuously Increasing Rigidity

A common generalization for the ground is an increasing rigidity with depth. The first model considers a ground with a linearly increasing Young's modulus,

$$E = E_0(1 + nz), \tag{13}$$

where E is Young's modulus, E_0 is the Young's modulus at the surface, z is the depth, and n determines the increase rate. The Poisson's ratio for the ground remains constant (Table 2). As the value of n increases the wave speeds increase faster with increasing depth solely due to the stiffness since we assume the density is constant. The surface deformations computed for a unit surface load is presented in Figure 9. The homogeneous model has a Young's modulus of the E_0 and represented by the $n = 0$ line. The displacements from both inhomogeneous and homogeneous models are close and convergent near the source. However,

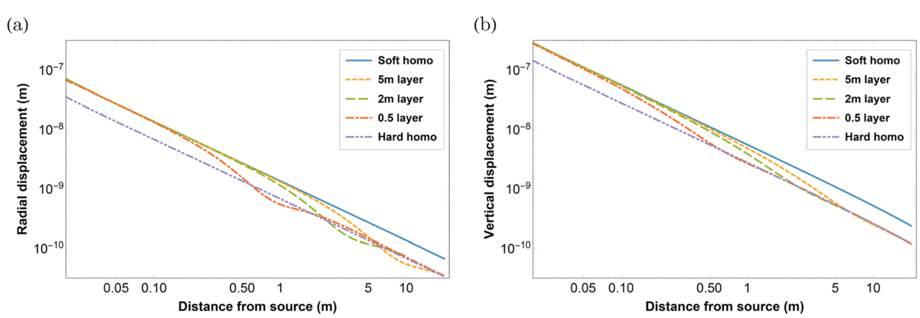

Figure 11. (a) Radial and (b) vertical surface displacements of a soft top layered ground of different thicknesses due to a unit vertical surface load.

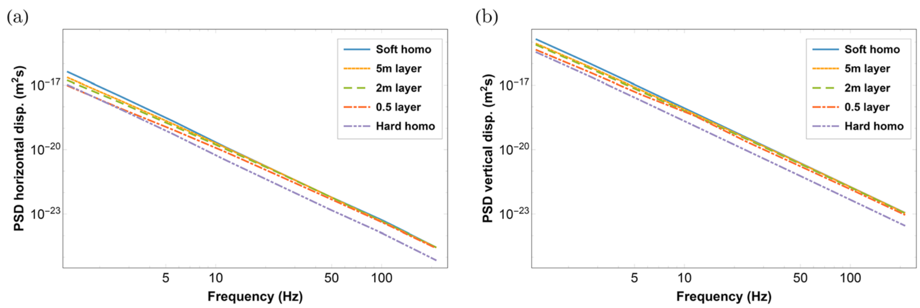

Figure 12. Predicted (a) horizontal and (b) vertical wind-induced displacements of a soft top layered ground of different thicknesses. PSD = power spectral density.

the surface displacements are smaller for the inhomogeneous model away from the source. The displacements decrease faster with increasing distance from the source as the rate of Young's modulus increases (larger n). An interpolating function is fitted on the computed data points from COMSOL. The generated response function is applied in the wind-ground equations, and the results are numerically calculated. The predicted wind-driven surface deformations for the homogeneous and inhomogeneous grounds are shown in Figure 10. At high frequency, all models predict similar wind-induced deformations. This suggests that at high frequency the resultant deformations are associated with disturbances closer to the measurement point. The differences at low frequencies increases and extends to higher frequencies as the rate of change of the Young's modulus (n) increases. Therefore, the influence of a gradually changing rigidity with depth is manifested in a changing slope of the PSD of wind coupling results. Since the slope changing occurs in the same fashion for both horizontal and vertical components, this ground structure does not increase the horizontal to vertical ratio to improve the agreement of the prediction with the wind-ground measurements.

4.2. Layered Ground

A model of an elastic layer over a homogeneous half-space subjected to a vertical static surface load is created in COMSOL having the soil properties representing a "soft soil" over a "hard soil" as listed in Table 3. The surface deformations for the ground having a soft soil layer over a hard soil half-space is shown in Figure 11. Three different layer thicknesses are considered to demonstrate the dependence on layer thickness. The limiting cases of a homogeneous soft soil and a homogeneous hard soil are also presented as reference. Both the vertical and radial displacements of the homogeneous half-spaces (hard and soft) decrease with distance from the source. They are parallel with a fixed difference in displacement (blue and purple lines in Figure 11). For the layered models, the displacements converge to the soft homogeneous half-space in the near field and gradually merge to the displacements of the hard homogeneous half-space in the far field. This change occurs at closer distances to the source for the models with a thinner layer. The layered grounds behave similar to a homogeneous ground made of the top layer material in the near field and similar to a homogeneous ground made of the bottom layer material in the far field.

The associated wind-driven deformations of the ground models are shown in Figure 12. The displacement PSDs approach the homogeneous model with top layer properties at high frequencies. As the frequency decreases, the layered models deviate from the homogeneous ground model with top layer properties toward

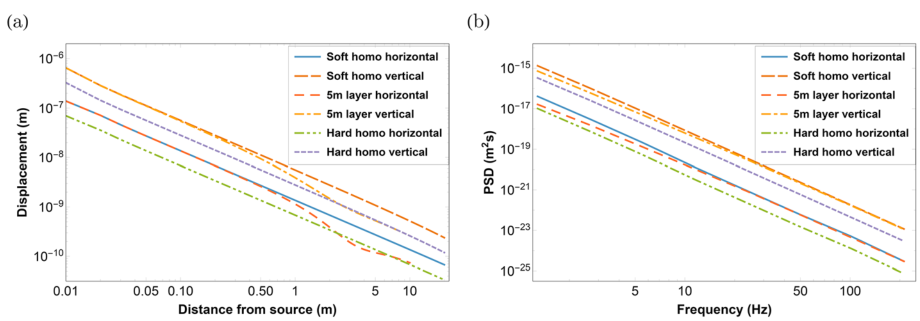

Figure 13. Predicted (a) displacements and (b) wind-induced displacements of homogeneous and layered ground models. PSD = power spectral density.

Table 4
Transversely Isotropic Model Parameters

E_r	E_z	ν_r	ν_{zr}	G_{rz}	Density
20 MPa	100 MPa	0.34	0.34	28 MPa	1,995 kg/m^3

the homogeneous model with the bottom layer properties. The deviation occurs at higher frequencies with decreasing the top layer thickness. This is consistent with the deformation versus range from the source. The wind-induced deformation of a layered ground behaves like a homogeneous ground with the upper layer properties at high frequencies. However, the sensitivity to the deeper layer properties increases with decreasing frequency and the sensitivity increases faster for thicker upper layers. This observation agrees with the general behavior of Rayleigh waves where the longer wavelengths penetrate deeper and are sensitive to deeper properties of the ground, whereas shorter wavelengths represent shallow properties.

The horizontal and vertical components of displacements and wind-driven displacements are compared in Figure 13. Based on the analytic solution for the homogeneous models, the radial to vertical displacement ratio is only a function of Poisson's ratio and is constant versus range and frequency. For the layered ground, the vertical and radial components change in the same fashion. Therefore, the current layering method (different Young's modulus) has no effect on the ratio of radial to vertical deformation and it remains constant versus range and frequency.

4.3. Anisotropic ground

A cross-anisotropic or transversely isotropic ground model is a half-space in which material properties have the same values in all directions parallel to the surface but different values perpendicular to the surface. This material is defined by five independent elastic constants. Equation (14) describes the elasticity matrix for a transversely isotopic material,

$$S = \begin{pmatrix} \frac{1}{E_r} & -\frac{\nu_r}{E_r} & -\frac{\nu_{zr}}{E_z} & 0 & 0 & 0 \\ -\frac{\nu_r}{E_r} & \frac{1}{E_r} & -\frac{\nu_{zr}}{E_z} & 0 & 0 & 0 \\ -\frac{\nu_{rz}}{E_r} & -\frac{\nu_{rz}}{E_r} & \frac{1}{E_z} & 0 & 0 & 0 \\ 0 & 0 & 0 & \frac{1}{G_{rz}} & 0 & 0 \\ 0 & 0 & 0 & 0 & \frac{1}{G_{rz}} & 0 \\ 0 & 0 & 0 & 0 & 0 & \frac{2(\nu_r+1)}{E_r} \end{pmatrix}, \tag{14}$$

where E_r and E_z are the Young's moduli in the plane of isotropy (horizontal) and in the normal direction, respectively. ν_r and ν_{zr} are Poisson's ratios characterizing the lateral strain response in the plane of isotropy to a stress acting parallel or normal to it, respectively. G_{rz} is the shear modulus in the normal direction to the surface (isotropic plane). Table 4 lists the elastic constants for a transversely isotropic ground model. For this case the Young's modulus in the vertical direction is greater than the Young's modulus in the horizontal directions indicating that the ground normal to the surface is stiffer than in the horizontal directions.

The vertical and radial surface displacements computed along a radial line from a unit vertical source is shown in Figure 14. The isotropic model uses a Young's modulus equal to E_r and a Poisson's ratio equal to ν_r.

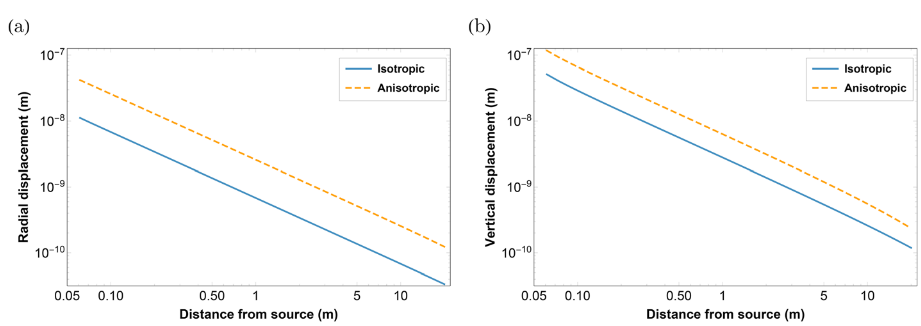

Figure 14. (a) Radial and (b) vertical surface displacements of isotropic and anisotropic ground models due to a unit vertical surface load.

10.1029/2019JB017562

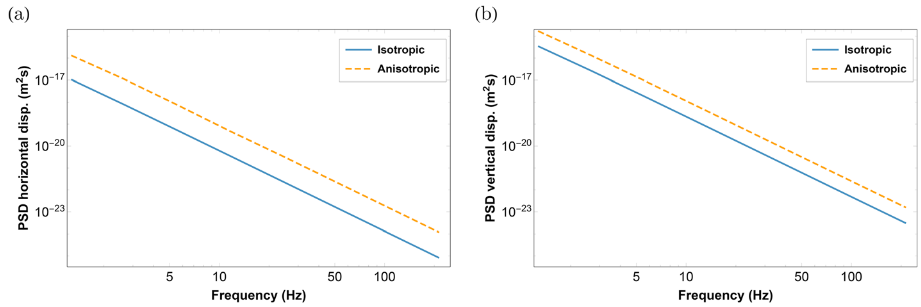

Figure 15. Predicted (a) horizontal and (b) vertical wind-induced displacements of isotropic and anisotropic ground models. PSD = power spectral density.

Both displacement components of the anisotropic model are greater than the isotropic model with the radial components having a larger difference. This is consistent with the wind-induced deformation predictions in Figure 15 where the radial component increase is bigger than the vertical component. Since anisotropy manifests in a magnitude shift of the PSD, it would not be possible to separate the effect of anisotropy from changes in elasticity. The predicted horizontal to vertical displacement ratio increases relative to the isotropic model. Although the ground model in the vertical direction is 5 times stiffer than that in the radial direction, the predicted horizontal wind-induced deformation is about 7% of the vertical deformation. This is an improvement over the homogeneous model but is not sufficient to agree with the measurements.

5. Conclusion

In the previous wind-ground coupling study, the ground was assumed to respond as an elastic isotropic homogeneous medium deforming quasi-statically due to the surface pressure caused by the wind. This work generalizes the ground model to include the dynamic response of the ground and the inhomogeneity and anisotropy of the ground.

The dynamic response of the ground as an elastic homogeneous half-space under the influence of a harmonic vertical surface load was obtained through analytical solution. A set of field measurements were conducted in order to measure the ground displacement under a harmonic load and to compare with the predictions. Although the results indicate general similarities in their trends, the measured amplitudes decay faster than the predicted values as a function of range and the rate of attenuation increases as a function of frequency. A linear viscoelastic model was introduced to account for losses. The closer prediction of viscoelastic model to the measurements demonstrates the effect of ground attenuations. In comparison to the static response of the ground surface, which has a constant and low radial to vertical deformation ratio, the dynamic response shows an oscillatory and increasing ratio with distance from the source. The dynamic prediction for wind-induced ground motion was introduced by replacing the static response with the dynamic response of the ground. Again, the vertical component of both the static and dynamic predictions are in a good agreement with the experiment. Although the horizontal displacements of the dynamic model show a slight increase compared to the static predictions, there is still a significant discrepancy between the predicted and measured displacements.

The response function for three different types of nonuniform grounds due to a vertical surface load was developed using Finite Elements (FE) modeling in COMSOL. The nonuniform models include inhomogeneous grounds with increasing rigidity with depth, layered grounds with an elastic layer over a half-space, and cross-anisotropic grounds. For the inhomogeneous grounds with different rates of increasing rigidity, the response functions are convergent near the source. However, they deviate based on the rigidity rate so that the response function decays faster with range as the rate increases. The wind-ground displacements predicted using the inhomogeneous models showed that the deformations of models are convergent at high frequencies. At low frequencies, the differences increase and extend to higher frequencies as the rate of change of rigidity increases. For layered grounds, the response function represents the elastic properties of the upper layer very close to the source and deviates toward representing the lower layer properties with increasing the distance. The deviation occurs faster and closer to the source for the grounds with thinner top layers. The associated wind-ground predictions represent the upper layer elastic properties at higher frequencies and deviate to represent the lower layer at very low frequencies. The different thicknesses of the top layer manifest in the rate of the deviation or the slope of the PSD lines which is higher for thinner top layers. The horizontal and vertical wind-induced displacements for the inhomogeneous ground models change in the same fashion compared to the homogeneous ones so that these kind of inhomogeneities do not improve the prediction of the horizontal component.

A transversely isotropic ground model with stiffer properties in the normal direction to the surface was built in COMSOL, and the surface response was applied to the wind-ground predictions. The final results show a small improvement of the horizontal to vertical displacement ratio relative to the uniform ground model.

This study showed that it is possible to have improved predictions for the horizontal component of wind-induced ground motion, even assuming no direct shear stress from the wind. However, the improvements are not enough to explain the difference between predictions and measurements. The calculations of this paper strongly indicate that the large horizontal displacements measured by Naderyan et al. (2016) are not due to either the dynamic response of the ground or the inhomogeneous nature of the ground.

This investigation also showed that the slope of the PSD of the wind-driven vertical deformations is sensitive to the ground structure and represents ground properties at different depths based on the frequency range of measurements. As future work, the sensitivity of wind-induced deformations to the ground structure can be investigated as a diagnostic method for ground inhomogeneities given the naturally occurring wind noise.

The remaining hypothesis in Naderyan et al. (2016) to be investigated is the assumption that the pressure field can be modeled as a stationary harmonic source characterized by the correlation functions measured by Shields (2005).

Acknowledgments
This work was supported by the U.S. Department of Agriculture under Non-Assistance Cooperative Agreement 58-6060-6-009. We appreciate the assistance of Gergo Arany and Leti Wodajo in the measurement program. The data published in this article can be obtained through the following link: https://egrove.olemiss.edu/ncpa_facpubs/1

References

Barkan, D. D. (1960). *Dynamics of bases and foundations*. New York: McGraw-Hill.

Booker, J., Balaam, N., & Davis, E. (1985). The behaviour of an elastic non-homogeneous half-space. Part I—Line and point loads. *International Journal for Numerical and Analytical Methods in Geomechanics*, *9*(4), 353–367.

Ernian, P. (1989). Static response of a transversely isotropic and layered half-space to general surface loads. *Physics of the Earth and Planetary Interiors*, *54*(3-4), 353–363.

Ewing, W. M., Jardetzky, W. S., Press, F., & Beiser, A. (1957). Elastic waves in layered media. *Physics Today*, *10*, 27.

Gerrard, C. (1982). Point and circular loads applied within a cross anisotropic elastic half space. *Applied Mathematical Modelling*, *6*(4), 262–272.

Kassir, M. (1970). The Reissner-Sagoci problem for a non-homogeneous solid. *International Journal of Engineering Science*, *8*(10), 875–885.

Lamb, H. (1904). On the propagation of tremors over the surface of an elastic solid. *Proceedings of the Royal Society of London*, *72*(477-486), 128–130.

Landau, L. D., & Lifshitz, E. M. (1986). *Theory of elasticity* (Vol. 7, pp. 109). New York: Elsevier.

Mohammadi, M. (2018). Elastodynamic model for wind induced ground motion (Master's thesis), University of Mississippi.

Naderyan, V., Hickey, C. J., & Raspet, R. (2016). Wind-induced ground motion. *Journal of Geophysical Research: Solid Earth*, *121*, 917–930. https://doi.org/10.1002/2015JB012478

Oner, M. (1990). Vertical and horizontal deformation of an inhomogeneous elastic half-space. *International Journal for Numerical and Analytical Methods in Geomechanics*, *14*(9), 613–629.

Pan, E., Bevis, M., Han, F., Zhou, H., & Zhu, R. (2007). Surface deformation due to loading of a layered elastic half-space: A rapid numerical kernel based on a circular loading element. *Geophysical Journal International*, *171*, 11–24. https://doi.org/10.1111/j.1365-246X.2007.03518.x

Panofsky, H., & Dutton, J. (1984). Atmospheric turbulence—Model and methods for engineering applications John Wiley and Sons New York 397 Google Scholar.

Reif, F. (1965). *Fundamentals of statistical and thermal physics*. New York: Mcgraw-Hill.

Shields, D. F (2005). Low-frequency wind noise correlation in microphone arrays. *The Journal of the Acoustical Society of America*, *117*(6), 3489–3496.

Wolfram Research Inc. (2018). *Mathematica, Version 11.3*. Champaign, IL.

Wang, C.-D., Pan, E., Tzeng, C.-S., Han, F., & Liao, J.-J. (2006). Displacements and stresses due to a uniform vertical circular load in an inhomogeneous cross-anisotropic half-space. *International Journal of Geomechanics*, *6*(1), 1–10.

Yu, J., Raspet, R., Webster, J., & Abbott, J. (2011). Wind noise measured at the ground surface. *The Journal of the Acoustical Society of America*, *129*(2), 622–632.

Yue, Z., & Wang, R. (1988). Static solution for transversely isotropic elastic N-layered systems. *Acta Scientiarum Naturalium, Universitatis Pekinensis*, *24*, 202–211.